J. Non-Newtonian Fluid Mech. 166 (2011) 487–499

Contents lists available at ScienceDirect

Journal of Non-Newtonian Fluid Mechanics

journal homepage: www.elsevier.com/locate/jnnfm

Shear cell rupture of nematic liquid crystal droplets in viscous fluids

Xiaofeng Yang[a,*], M. Gregory Forest[b], Chun Liu[c], Jie Shen[d]

[a] Department of Mathematics, University of South Carolina, Columbia, SC 29083, United States
[b] Department of Mathematics, Institute for Advanced Materials, Nanoscience & Technology, University of North Carolina at Chapel Hill, Chapel Hill, NC 27599-3250, United States
[c] Department of Mathematics, Pennsylvania State University, University Park, PA 16802, United States
[d] Department of Mathematics, Purdue University, West Lafayette, IN 47907, United States

ARTICLE INFO

Article history:
Received 22 March 2010
Received in revised form 11 February 2011
Accepted 14 February 2011
Available online 19 February 2011

Keywords:
Phase-field
Multi-phase
Complex fluids
Liquid crystal

ABSTRACT

We model the hydrodynamics of a shear cell experiment with an immiscible nematic liquid crystal droplet in a viscous fluid using an energetic variational approach and phase-field methods [86]. The model includes the coupled system for the flow field for each phase, a phase-field function for the diffuse interface and the orientational director field of the liquid crystal phase. An efficient numerical scheme is implemented for the two-dimensional evolution of the shear cell experiment for this initial data. The same model reduces to an immiscible viscous droplet in a viscous fluid, which we simulate first to compare with other numerical and experimental behavior. Then we simulate drop deformation by varying capillary number (independent of liquid crystal physics), liquid crystal interfacial anchoring energy and Oseen–Frank distortional elastic energy. We show the number of eventual droplets (one to several) and "beads on a string" behavior are tunable with these three physical parameters. All stable droplets possess signature quadrupolar shear and normal stress distributions. The liquid crystal droplets always possess a global surface defect structure, called a boojum, when tangential surface anchoring is imposed. Boojums [79,32] consist of degree +1/2 and −1/2 surface defects within a bipolar global orientational structure.

1. Introduction

Moving interface problems are ubiquitous in the study of mixtures of fluids, solids and gases. Many problems in the biological, physical and engineering sciences involve systems of equations that need to be solved in evolving domains with complex interfaces. This paper is motivated by composite material applications where liquid crystal domains are dispersed in an immiscible polymer phase and then sheared to create arrays of liquid crystal droplets [46,80]. In the classical sharp interface formulation, the model system consists of the momentum equations for each fluid region, supplemented by the kinematic and dynamic boundary conditions on the free interfaces [5,8,14,33,58].

The available numerical methods for solving free-interface problems can roughly be divided into two categories, those of Lagrangian formulations and those of Eulerian formulations. Recognized as an explicit tracking method of the interface, Lagrangian methods track the interface either through a separate grid for the interface, or a set of interconnected "marker" points. Examples include boundary integral methods (surface mesh [6,27,78,30,9]) and the front-tracking method (a set of connected marker particles [19,52,75,83,89]). Lagrangian approaches are typically very accurate, but can be relatively complicated to implement, especially for problems involving drastic topological changes; we refer to [9] for an adaptive mesh algorithm applied to three-dimensional drop deformation and breakup.

In Eulerian methods, the interface is implicitly defined through a "label" function, sometimes referred to as the level set function or phase field, with an evolution equation for the label function that is supposed to mimic the physics of the explicit interface. A particular value (level set) of the label function is defined as the interface. The numerical solution can be performed independently of the underlying grid, which greatly simplifies gridding, discretization and handling of topological changes. Examples include the volume-of-fluid (VOF) method [26,31,38,22,47], level-set method [1,54,65], immersed boundary method [55,39] and the phase-field method which we use in this study.

The phase-field, or diffuse-interface, method dates back to Rayleigh and van der Waals in the 19th century [62,77]; we refer to the monograph by Rowlinson and Widom [64] and review article by Anderson et al. [2] for historical developments and diverse applications of these methods. The diffuse interface, for our purposes here of modeling immiscible drops of one fluid in another, represents a transition layer where the two fluids mix to a cer-

* Corresponding author. Tel.: +1 803 777 3776; fax: +1 803 777 6527.
E-mail addresses: xfyang@math.sc.edu, xfyang@email.unc.edu (X. Yang), forest@amath.unc.edu (M.G. Forest), liu@math.psu.edu (C. Liu), shen@math.purdue.edu (J. Shen).

0377-0257/$ – see front matter © 2011 Elsevier B.V. All rights reserved.
doi:10.1016/j.jnnfm.2011.02.004

tain degree, governed by a mixing energy. The governing equations arise from a standard energetic variational procedure including the Hamilton least action principle (for reversible processes) and the Onsager maximum dissipation principle (for irreversible processes) [44,40,29]. Phase-field models provide a robust and flexible treatment for interfacial dynamics of multi-phase flows; we refer the reader to several examples from the physics and engineering literature (cf. [88,92,90,82,13]).

The study of immiscible fluid mixtures dates back to the work of Plateau [56] and Rayleigh [61], with relatively modern studies of Taylor [74], Hinch and Acrivos [25] and Rallison [59]. Advances in instrumentation and computation have facilitated further contributions to understanding a particular two-phase flow, the falling drop experiment, where there is a free surface bounding one fluid and a gas that is assumed passive. Studies of the deformation, formation and pinch-off of a Newtonian drop have been reported with experimental [71,24,91,81,30,23], theoretical [71,24,15,7], and numerical [71,81,23,6,38,43] tools (for a thorough review of the subject see [16,10]). When the fluid is non-Newtonian, observations are often dramatically altered. In the dripping faucet, much longer filaments form between the drop and the orifice for polymeric liquids [3,4,16]. Many studies, both experimental and theoretical, were devoted to study the equilibrium shape [28,60,43], the critical conditions for breakup [37,18,76] and capillary instability [76] of viscoelastic drops. New features due to elasticity of the fluid have been documented, such as filament stabilization, (elastic) retraction, extraordinary long and long-lived filament formation and the development of beads-on-a-string perturbations along the filament [20,53,73,63,72]. The dynamics during and after filament rupture continue to be explored for fundamental behavior as well as for applications to ink jet and related technologies. A high-resolution simulation of inkjet printing of polymeric liquids can be found in [51], which also contains a detailed discussion of their numerical methods and polymer modeling.

In this paper we explore an immiscible liquid crystal (LC) droplet immersed in a viscous fluid confined between two parallel plates, and simulate the fate of the LC droplet and feedback to the surrounding fluid motion as the plates are set into steady motion to generate a bulk shear flow. There are various applications which motivate this modeling study, including polymer-dispersed liquid crystals mentioned above where the viscous matrix considered here has to be generalized to a polymeric fluid. It seems prudent to address the simpler problem first, then replace the viscous matrix by any polymer model with an energy formulation. The LC droplet requires, minimally, the computation of the orientation within the liquid crystal phase with some model of the nematic director dynamics and elastic fluid properties. Previous studies of liquid crystal drops have focused on a uniform or varying external electric field (cf. [17,36] and references therein), magnetic field [57], or external shear flow [48,34,87]. We follow the formalism for two-phase complex fluids developed in [86]. This work provides a general framework for complex fluid mixtures where the microstructural dynamics has an energy-based variational basis. In [86], the authors illustrated the formalism for the slow retraction of a nematic liquid crystal (LC) drop in a viscous solvent, where both fluids are highly viscous. Here we extend the model and numerical algorithm to the inertial regime where the LC drop undergoes strong deformation and rupture, and where defects in the LC phase and hydrodynamic effects are of interest in their own right.

We draw special attention to the role of defects in the liquid crystal phase during drop deformation and rupture, the secondary flow and stress distributions of stable drops, and their correlations with defects. Defects are classified according to topological degree which is calculated by an integral relation that is performed on a closed curve surrounding the core of the defect; for half-integer or integer defects, respectively, the director rotates through multiples of π or 2π radians. The defect topology of a nematic liquid crystal drop, both in equilibrium and in hydrodynamics, depends critically on the nature of the orientational boundary conditions at the drop interface. The standard assumption is that of Dirichlet conditions at interfaces, so-called hard anchoring conditions. Within the phase field approach taken here, we restrict this study to tangential anchoring and then parametrically tune the strength of the anchoring condition through an anchoring energy, which we show plays a dominant role in the global orientation field within LC droplets.

The rest of the paper is arranged as follows. In Section 2, we describe the basic setting and model equations. In Section 3, the corresponding numerical scheme is presented. Numerical simulations are presented and highlights summarized in Section 4, followed by concluding remarks.

2. The phase-field model of two-phase complex fluids

Let Ω be a domain which is filled by two incompressible and immiscible fluids separated by a free moving interface. In our study, we initialize a liquid crystal drop within a viscous fluid. To distinguish these two fluids, a phase field function $\phi(x)$ with $x \in \Omega$ is introduced and the level set $\{x : \phi(x) = 0\}$ depicts the interface, while $\{x : \phi(x) > 0\}$ represents the interior and $\{x : \phi(x) < 0\}$ the exterior. Since this labeling function is defined on the whole domain with the Eulerian referenced coordinates, we evolve the full phase field function ϕ and plot the motion of the zero level set to identify the fluid–fluid interface.

We now establish a phase field formulation based on an energetic variational approach [86,40,85]. For the system of an immiscible blend of a nematic liquid crystal droplet and a viscous matrix, there are three contributions to the free energy: the mixing energy F_{mix} of the interface, the bulk distortional energy F_{bulk} of the nematic liquid crystal phase, and the anchoring energy F_{anch} of the liquid crystal phases on the interface. If we suppress the latter two free energy contributions, then we reduce to the standard Cahn–Hilliard or Allen–Cahn models for two-phase immiscible fluids.

An order parameter η is used to represent the thickness of the thin mixing layer separating the two fluids. The evolution of the phase field function is governed by a stored *mixing energy* density [12] given by

$$f_{mix}(\phi, \nabla\phi) = \frac{1}{2}\lambda|\nabla\phi|^2 + \frac{\lambda}{4\eta^2}(\phi^2 - 1)^2, \tag{2.1}$$

where λ *is the strength of the mixing energy*. The first gradient term represents the "philic" interactions between the fluids which prefer complete mixing. The second term is the Ginzburg–Landau potential for "phobic" interactions that promotes phase separation of the two fluids. Notice that ϕ is +1 for the nematic fluid, −1 for the ambient fluid, with a transitional layer width of order $O(\eta)$.

For two-phase Newtonian (purely viscous) fluids, the free energy above yields the Cahn–Hilliard or Allen–Cahn equation depending on the choice of Banach space to derive the variational derivative [86,40,85].

The nematic liquid crystal fluid, whose principal axis of orientation is represented by a unit vector $\mathbf{n}(x)$ known as the LC director, possesses an additional elastic energy given by the Oseen–Frank distortional energy density

$$f_{bulk}(\mathbf{n}) = \frac{1}{2}K_1(\nabla\cdot\mathbf{n})^2 + \frac{1}{2}K_2(\mathbf{n}\cdot\nabla\times\mathbf{n})^2 + \frac{1}{2}K_3(\mathbf{n}\times\nabla\times\mathbf{n})^2, \tag{2.2}$$

where K_1, K_2, K_3 are elastic constants for the three canonical orientational distortions: splay, twist and bend. For simplicity, we assume the elastic energy of the liquid crystal droplet is isotropic,

i.e., $K_1 = K_2 = K_3 = K$, and the Oseen–Frank energy density reduces to the Dirichlet functional $K/2\,\nabla\mathbf{n}:(\nabla\mathbf{n})^T$. Furthermore, rather than impose a norm 1 constraint directly on $\mathbf{n}$, instead we introduce a penalty term of Ginzburg–Landau type, $1/4\varepsilon^2(|\mathbf{n}|^2-1)^2$, where $\varepsilon \ll 1$ is a penalization parameter. Then the "regularized" bulk elastic energy density becomes [42]

$$f_{bulk} = \frac{1}{2}K\nabla\mathbf{n}:(\nabla\mathbf{n})^T + \frac{(|\mathbf{n}|^2-1)^2}{4\varepsilon^2}. \tag{2.3}$$

This formulation circumvents the incapacity of the Oseen–Frank theory to describe the core of defects through a transition zone with width of order $O(\varepsilon)$ [42,41]. This effect will be evident in the simulations below as the director shrinks from norm 1 in the vicinity of a defect core. The alternative approach is to generalize the LC director to a tensorial order parameter or the full orientational distribution function, which is beyond the scope of this paper.

Liquid crystals tend to prefer a particular orientation along an interface, called the easy direction. In sharp interface models this constitutes a so-called hard anchoring (Dirichlet) boundary condition for $\mathbf{n}$. In the phase field approach, instead one employs an *anchoring energy* which can measure the deviations from the preferred interfacial alignment condition. The two most common types of anchoring are planar, where all directions in the plane of the interface are easy directions, and homeotropic, where the easy direction is the normal to the interface. The natural energy density for the planar anchoring case is

$$f_{anch}(\mathbf{n},\phi) = \frac{1}{2}A(\mathbf{n}\cdot\nabla\phi)^2, \tag{2.4}$$

where $A \geq 0$ is a parameter controlling the strength of the anchoring potential. For the normal anchoring case, the energy density is

$$f_{anch}(\mathbf{n},\phi) = \frac{1}{2}A(|\mathbf{n}|^2|\nabla\phi|^2 - (\mathbf{n}\cdot\nabla\phi)^2). \tag{2.5}$$

The total energy density is then a sum,

$$f_{tot}(\phi,\mathbf{n},\nabla\phi,\nabla\mathbf{n}) = f_{mix} + \frac{1}{2}(1+\phi)f_{bulk} + f_{anch}, \tag{2.6}$$

where the factor $(1+\phi)/2$ represents the volume fraction of the nematic liquid crystal component. Note that the last two contributions vanish in the viscous liquid phase (by setting $\phi = -1$ and $A = 0$). The total free energy is

$$F_{tot} = \int_\Omega f_{tot}(\phi,\mathbf{n},\nabla\phi,\nabla\mathbf{n})dx. \tag{2.7}$$

Note that the free energy F_{tot} is parametrized by the diffuse interface mixing parameter λ and interfacial width η, and by LC parameters for bulk elasticity K, director norm constraint ε, and surface anchoring strength A. We now couple this energy to the flow equations.

The momentum conservation and continuity equations are

$$\rho\left(\frac{\partial\mathbf{u}}{\partial t} + \mathbf{u}\cdot\nabla\mathbf{u}\right) = -\nabla p + \nabla\cdot\sigma,\ \nabla\cdot\mathbf{u} = 0, \tag{2.8}$$

where ρ is the density, $\mathbf{u}$ is the velocity, p is the pressure and σ is the stress. In this paper we assume both fluids are density matched. The elastic stress tensor is derived from the total elastic energy above through the least action principle [11],

$$\sigma^e = -\lambda(\nabla\phi\otimes\nabla\phi) - \frac{K}{2}(1+\phi)(\nabla\mathbf{n})\cdot(\nabla\mathbf{n})^T - G, \tag{2.9}$$

where $G = A(\mathbf{n}\cdot\nabla\phi)\mathbf{n}\otimes\nabla\phi$ for planar anchoring (chosen in this paper) and $G = A((\mathbf{n}\cdot\mathbf{n})\nabla\phi - (\mathbf{n}\cdot\nabla\phi)\mathbf{n}]\otimes\nabla\phi$ for normal anchoring. As in [86], we suppress director torque due to flow in the liquid crystal director model, and neglect the terms that represent anisotropic viscous extra stress contributions. These terms and effects are considered perturbative to the model we explore here and will be studied separately. The Newtonian viscous stress for both fluids is

$$\sigma^v = \mu(\nabla\mathbf{u} + (\nabla\mathbf{u})^T), \tag{2.10}$$

where μ is the viscosity of either fluid, which we assume to be matched for this paper. The total stress tensor is the summation of the elastic stress σ^e and the viscous stress σ^v.

Based on the total free energy of the system, the Cahn–Hilliard equation arises as the evolution equation of the labeling function ϕ with a particular choice of Banach space norm, which is the choice we make for this paper. That is, we turn off the liquid crystal contributions in the evolution of the phase field function, which is standard in the literature; if the model performs poorly with this assumption, this is one place to look to add new physics. For the liquid crystal droplet experiments, we focus our simulations on the phase field (parametrized by λ) and LC (parametrized by K and A) contributions to the elastic stress, which strongly couple to the flow equations.

The Cahn–Hilliard phase field model (employed in all simulations presented here) is

$$\phi_t + \mathbf{u}\cdot\nabla\phi = \nabla\cdot\gamma_1\nabla\left(\frac{\delta F_{mix}}{\delta\phi}\right) = \gamma_1\lambda\nabla^2\left(-\nabla^2\phi + \frac{\phi(\phi^2-1)}{\eta^2}\right), \tag{2.11}$$

where the parameter γ_1 is the so-called molecular mobility constant, and $\gamma_1\lambda$ determines the relaxation time scale of the interface. We assume a no-flux boundary condition on the full fluid domain Ω,

$$\frac{\partial\phi}{\partial n}|_{\partial\Omega} = 0. \tag{2.12}$$

The second boundary condition comes from the variational principle [40,44],

$$\frac{\partial\nabla^2\phi}{\partial n}|_{\partial\Omega} = 0. \tag{2.13}$$

We point out that as an alternative transport equation of the phase field (2.11), we can use the Allen–Cahn equations:

$$\phi_t + \mathbf{u}\cdot\nabla\phi = -\gamma_1\left(\frac{\delta F_{mix}}{\delta\phi}\right) = -\gamma_1\lambda\left(-\nabla^2\phi + \frac{\phi(\phi^2-1)}{\eta^2}\right), \tag{2.14}$$

with the no-flux boundary condition (2.12) and the second boundary condition (2.13) is dropped. The Allen–Cahn equation involves a dissipation of the volume fraction for which one can introduce a Lagrange multiplier to restore conservation [85,68]. We do not pursue this model here.

The evolution equation for the director field n is determined by the variational derivative of the bulk free energy,

$$\mathbf{n}_t + \mathbf{u}\cdot\nabla\mathbf{n} = -\gamma_2\frac{\delta((1+\phi)/2\,F_{bulk})}{\delta\mathbf{n}} = \gamma_2 K\left(\nabla\cdot\left(\frac{(1+\phi)}{2}\nabla\mathbf{n}\right) - \frac{(1+\phi)}{2}\frac{\mathbf{n}(|\mathbf{n}|^2-1)}{\varepsilon^2}\right) + \gamma_2 Ag, \tag{2.15}$$

where $g = (\mathbf{n}\cdot\nabla\phi)\nabla\phi$ for planar anchoring, and $(\nabla\phi\cdot\nabla\phi)\mathbf{n} - (\mathbf{n}\cdot\nabla\phi)\nabla\phi$ for normal anchoring, and γ_2 determines another relaxation time scale of the liquid crystal phase. For simplicity, we assume a Neumann boundary condition on the LC director $(\partial n/\partial n)|_{\partial\Omega} = 0$. In this way, we allow the director field to freely decay to zero in the exterior region of the drop by the effects from the volume fraction factor $(1+\phi)/2$.

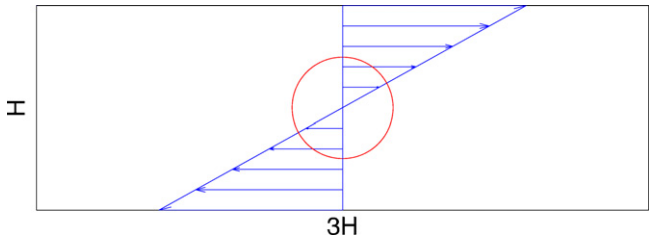

Fig. 1. Initial data of a drop of one fluid immersed in another fluid, subjected at time 0 to an imposed linear shear. The red circle is the zero level set of a phase field function which will be subsequently tracked for different two-fluid experiments. (For interpretation of the references to color in this figure legend, the reader is referred to the web version of the article.)

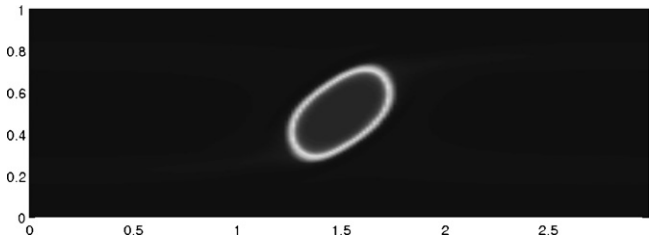

Fig. 2. Steady state shape of a sheared Newtonian drop in a Newtonian fluid at a sub-critical capillary number with $Ca = 0.0486$.

3. Numerical method

We start by describing our time discretization scheme. We advance time semi-implicitly to enhance stability, with the nonlinear transport terms treated explicitly and the linear terms implicitly. The incompressibility constraint is dealt with by using

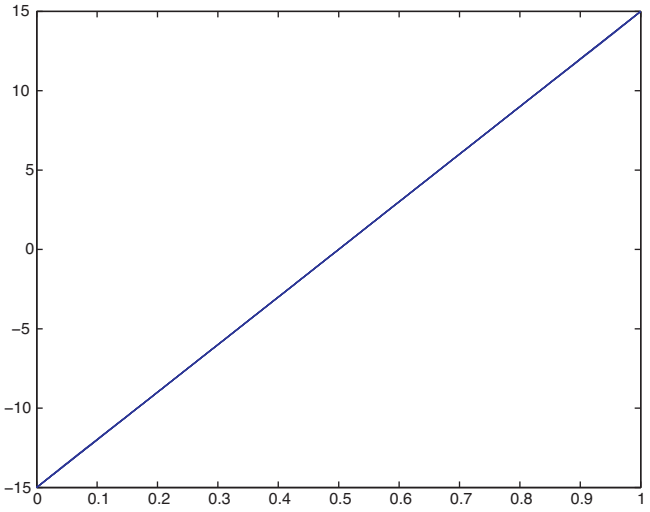

Fig. 4. The velocity profile of u at $t = 0.1, 0.4, 0.7, 0.9, 1, 1.1$ corresponding to Fig. 3.

the rotational pressure–correction scheme developed in [21]. More precisely, assuming $(u^n, p^n, \phi^n, \mathbf{n}^n)$ are known, we solve $(u^{n+1}, p^{n+1}, \phi^{n+1}, \mathbf{n}^{n+1})$ as follows:

$$\frac{\tilde{u}^{n+1} - u^n}{\delta t} - \mu\nabla^2\tilde{u}^{n+1} + \nabla p^n = g^n, \quad \tilde{u}^{n+1}|_{\partial\Omega} = 0; \tag{3.1a}$$

$$-\nabla^2\psi^{n+1} = \frac{1}{\delta t}\nabla\cdot\tilde{u}^{n+1}, \quad \frac{\partial\psi^{n+1}}{\partial n}|_{\partial\Omega} = 0; \tag{3.1b}$$

and

$$p^{n+1} = p^n + \psi^{n+1} - \mu\nabla\cdot\tilde{u}^{n+1}, \quad u^{n+1} = \tilde{u}^{n+1} - \delta t\nabla\psi^{n+1}; \tag{3.1c}$$

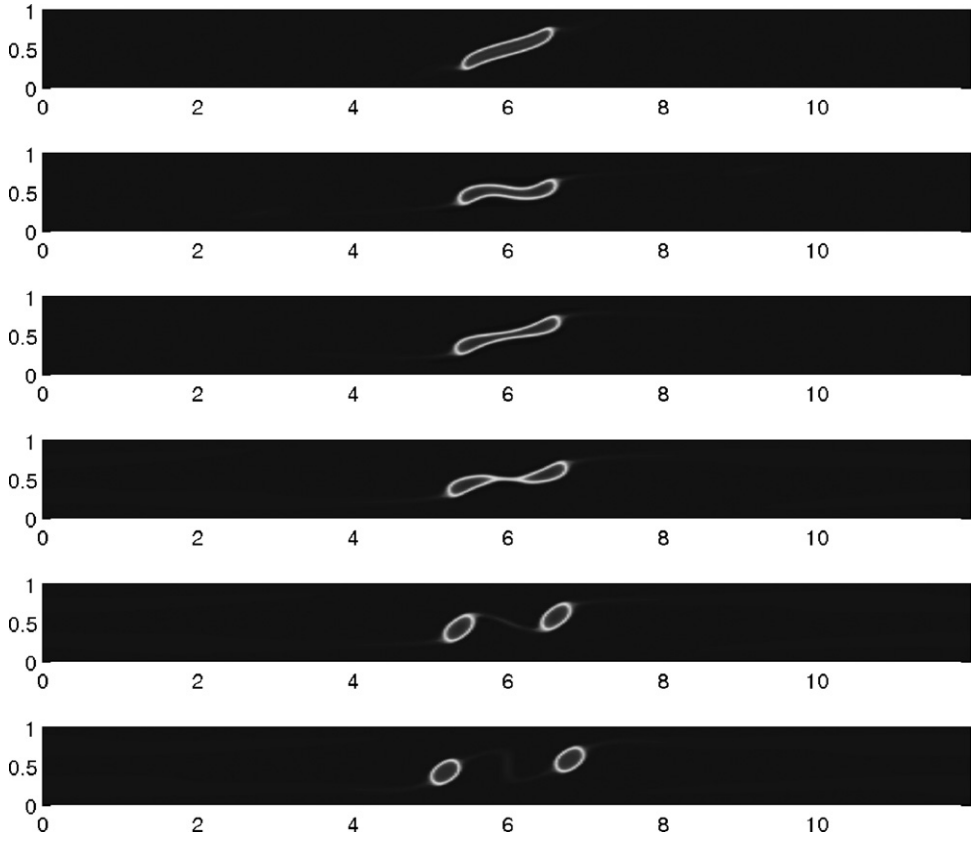

Fig. 3. Snapshots of the deformation of a Newtonian drop that is immersed in a Newtonian fluid, at $t = 0.1, 0.4, 0.7, 0.9, 1, 1.1$ with shear rate $\kappa = 15$ with domain size $[0,12] \times [0,1]$.

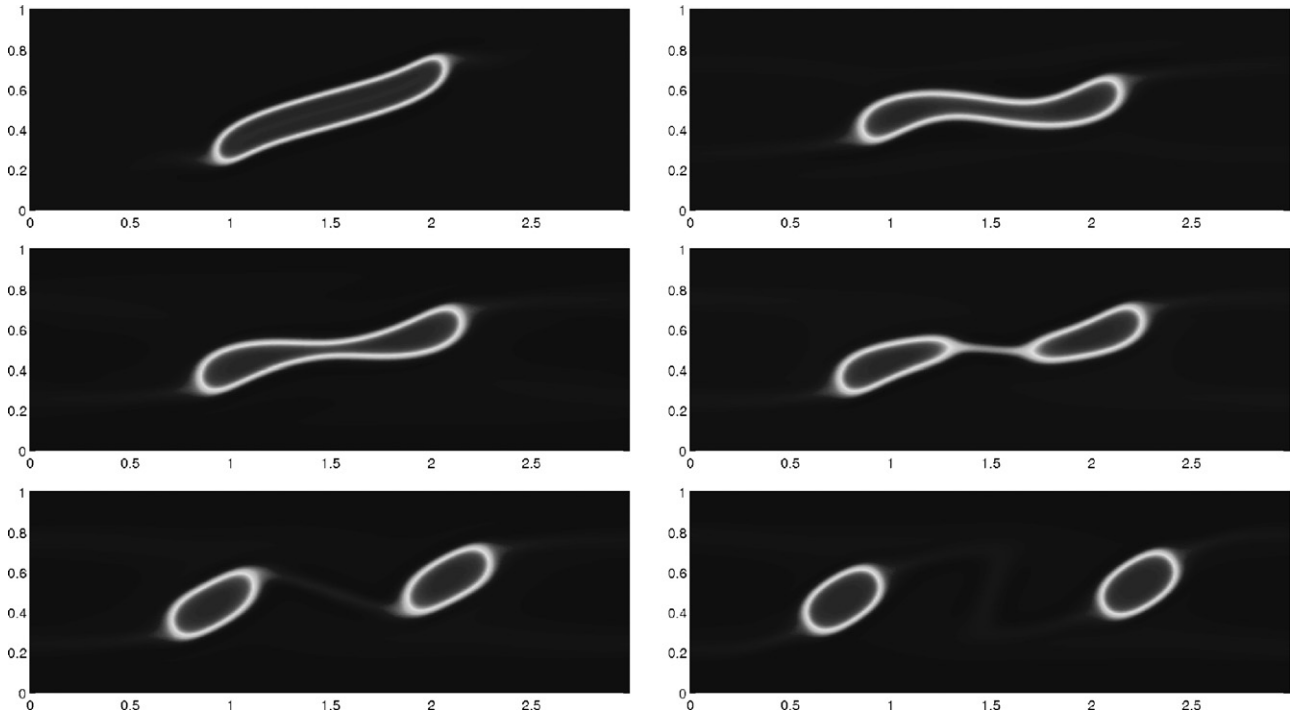

Fig. 5. Snapshots of the deformation of a viscosity matched, immiscible Newtonian drop immersed in a Newtonian fluid, at $t = 0.1, 0.5, 0.7, 0.83, 0.89, 1$ with $[0,3] \times [0,1]$.

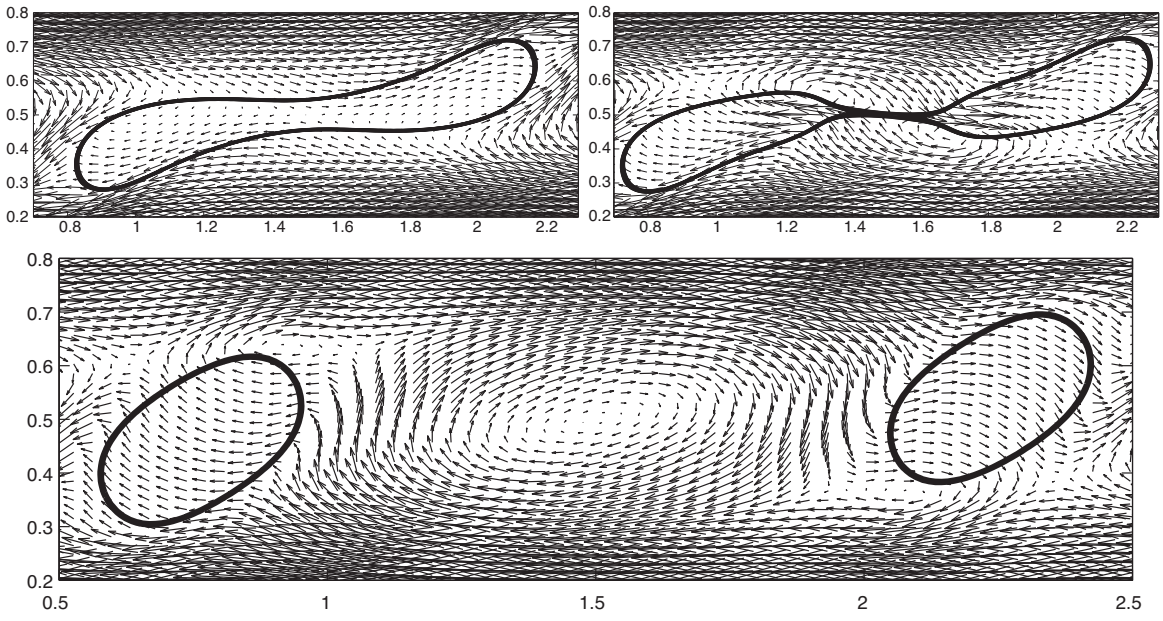

Fig. 6. Snapshots of the velocity field with phase-field contours of the Newtonian drop at $t = 0.7, 0.83, 1$, associated with the drop dynamics of Fig. 5.

$$\frac{\phi^{n+1}-\phi^n}{\gamma_1\lambda\delta t}+\nabla^2\nabla^2\phi^{n+1}-\frac{S_\phi}{\eta^2}\nabla^2(\phi_{n+1}-\phi_n)=\nabla^2 f(\phi^n),$$

$$\frac{\partial\phi_{n+1}}{\partial n}|_{\partial\Omega}=0,\ \frac{\partial\nabla^2\phi_{n+1}}{\partial n}|_{\partial\Omega}=0; \tag{3.2}$$

and

$$\frac{\mathbf{n}^{n+1}-\mathbf{n}^n}{\gamma_2 K\delta t}-\nabla^2(\mathbf{n}^{n+1}-\mathbf{n}^n)+\frac{S_{\mathbf{n}}}{\varepsilon^2}(\mathbf{n}^{n+1}-\mathbf{n}^n)=\nabla$$

$$\cdot(\frac{1}{2}(1+\phi^n)\nabla\mathbf{n}^n)-\frac{1}{2}(1+\phi^n)\frac{\mathbf{n}^n(|\mathbf{n}^n|^2-1)}{\varepsilon^2},\ \frac{\partial\mathbf{n}^{n+1}}{\partial n}|_{\partial\Omega}=0. \tag{3.3}$$

In the above, g^n inlcudes all the nonlinear terms in (2.9) evaluated at time step n; S_ϕ, $S_n > 0$ are two suitable stabilization parameters. In our numerical simulations, we use $S_\phi = S_n = 2$ which appear to provide a good balance between stability and accuracy. Details of stability and error analysis of this stabilized semi-implicit scheme can be found in [84,69].

Note that the second order term in (2.15) involves a non-constant coefficient $(1+\phi)/2$, and since $\phi \sim -1$ in the exterior of the drop, $\phi + 1$ oscillates around zero. Hence, $(\phi + 1)$ may become negative at some grid points which can cause an iterative method like Conjugate Gradient method to diverge. The situation is avoided by

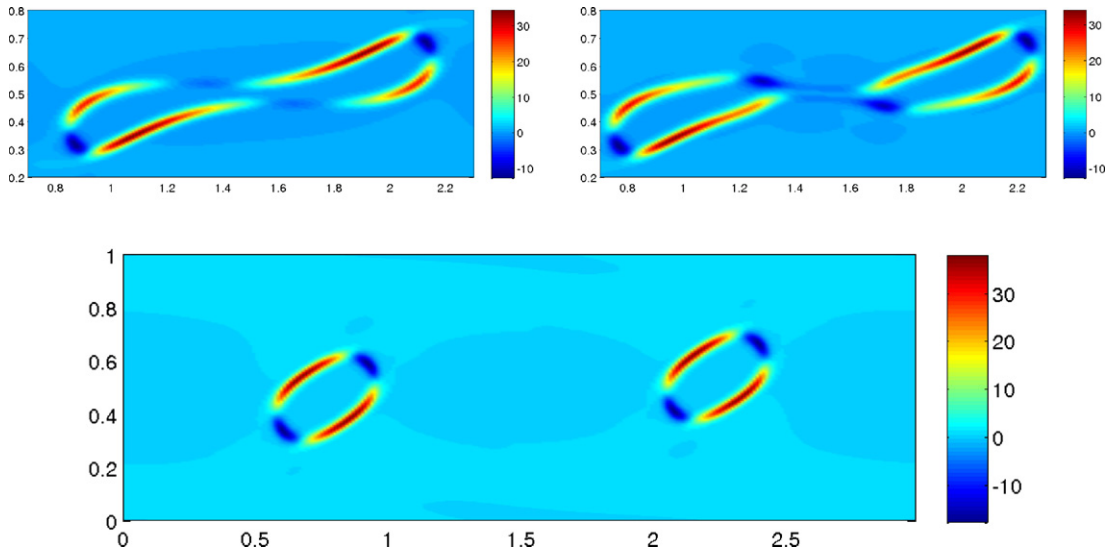

Fig. 7. The shear stress σ_{12} associated with the snapshots from Fig. 6 at $t = 0.7, 0.83, 1$.

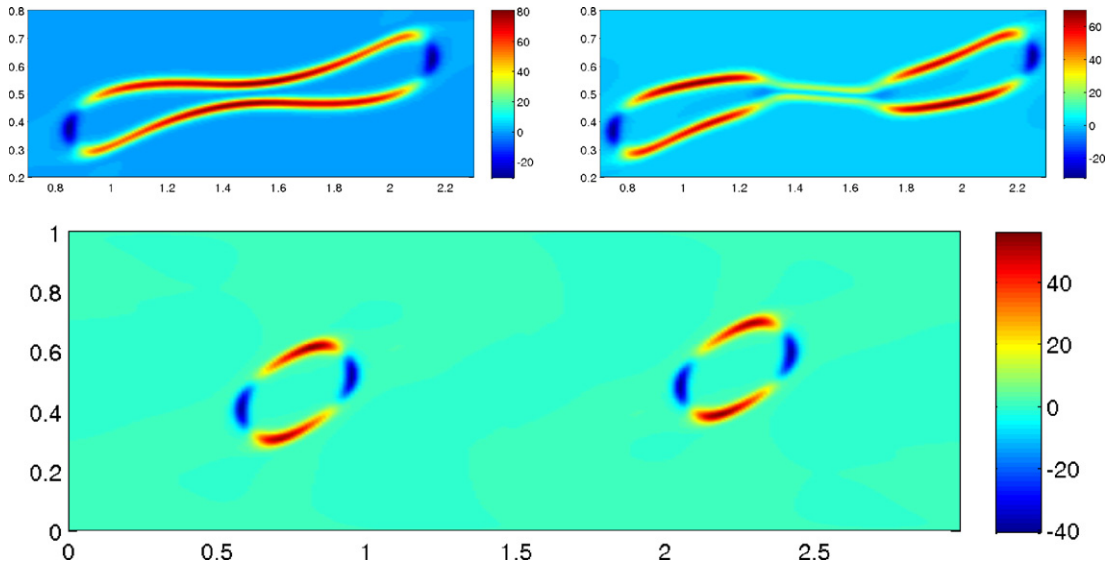

Fig. 8. The first normal stress difference $N_1 = \sigma_{11} - \sigma_{22}$ corresponding to the snapshots of Figs. 6 and 7.

a standard approximation of the second-order operator with variable coefficients by one with constant coefficients, as evident in (3.3).

To summarize, at each time step, the above scheme leads to a sequence of Poisson-type equations for u^{n+1}, p^{n+1}, $\mathbf{n}^{n+1}$ and a bi-harmonic equation for ϕ^{n+1}. Since these equations have constant coefficients and the domain is regular, they can be efficiently and accurately solved by using a spectral-Galerkin method (cf. [66]). More precisely, we consider the two-dimensional rectangular domain $\Omega = \{(x, y) : x \in [0, H_x], y \in [0, H_y]\}$ with periodic boundary conditions along the x-axis. We apply a Fourier spectral method in the x-direction (i.e., periodicity in the flow direction) and the Legendre–Galerkin method (cf. [66]) in the y-direction, to resolve the physical boundary conditions at the upper and lower plates. We note in particular that, in order to reduce the computational complexity, we use the basis functions which satisfy exactly the Neumann boundary condition for the director field n, as well as the boundary conditions (2.12) and (2.13) for the Cahn–Hilliard equation [66]. For these basis functions, the resultant linear systems from the scheme are all sparse with compact bandwidth so they can be solved with optimal computational complexity.

4. Numerical simulations

4.1. Problem formulation

We now investigate the drop deformation problem in a shear cell where the plates will be set into steady motion, imposing a bulk shear rate on the fluid mixture. In all computations, the initial geometry is depicted schematically in Fig. 1. The computational domain is the rectangle with lengths $H_x = 3H$, $H_y = H$ and $H = 1$. The drop sits in the center with a radius of $a = (H/4)$. The plate-controlled bulk shear rate is κ, and κ^{-1} defines a characteristic time scale. We use H as the characteristic length scale. In all simulations, we fix the following parameters based on trial and error and previous experience with a drop retraction application [86,40,85]:

- the mobility parameter of the phase field variable, $\gamma_1 = 2 \times 10^{-5}$;

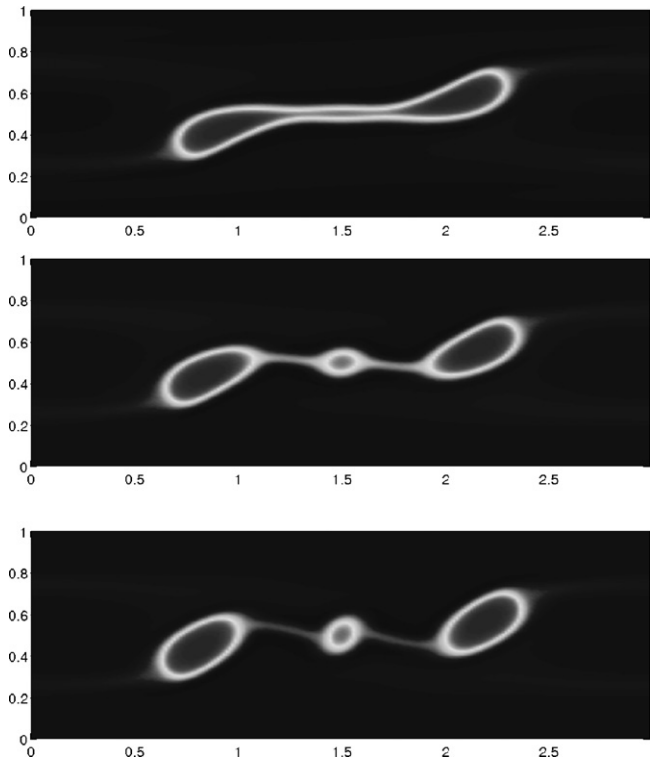

Fig. 9. Snapshots of a sheared liquid crystal drop in a viscous ambient fluid with bulk Frank energy constant of $K = 0.05$ and zero anchoring energy ($A = 0$) at $t = 0.88$, 0.97, 1.

- the relaxation rate parameter of the LC director, $\gamma_2 = 0.02$;
- the phase field mixing energy parameter, $\lambda = 0.047$;
- the diffuse interface capillary width parameter, $\eta = 0.02$;
- the LC director norm 1 penalty parameter $\varepsilon = 0.03$;
- both fluid phases have the same viscosity $\mu = 1/30$ and density $\rho = 1$.

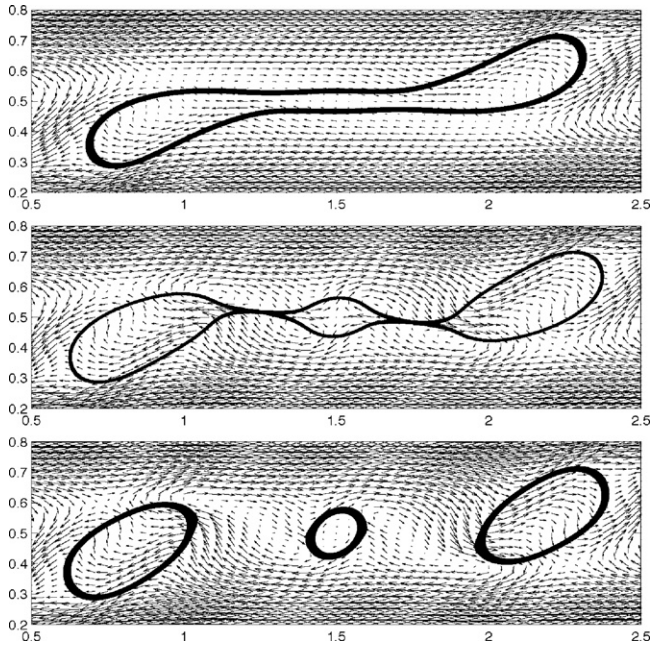

Fig. 10. The velocity field superimposed with the level set $\{x : \phi(x) = 0\}$ corresponding to Fig. 9.

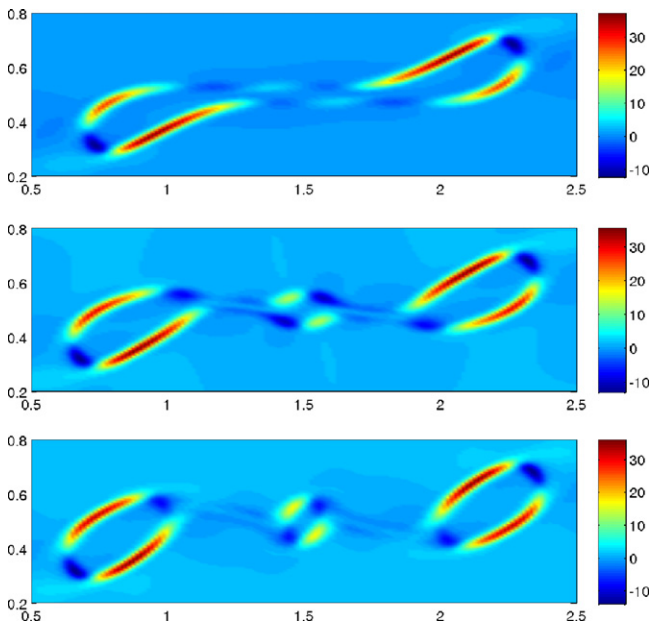

Fig. 11. Shear stress distributions σ_{12} corresponding to Figs. 9 and 10.

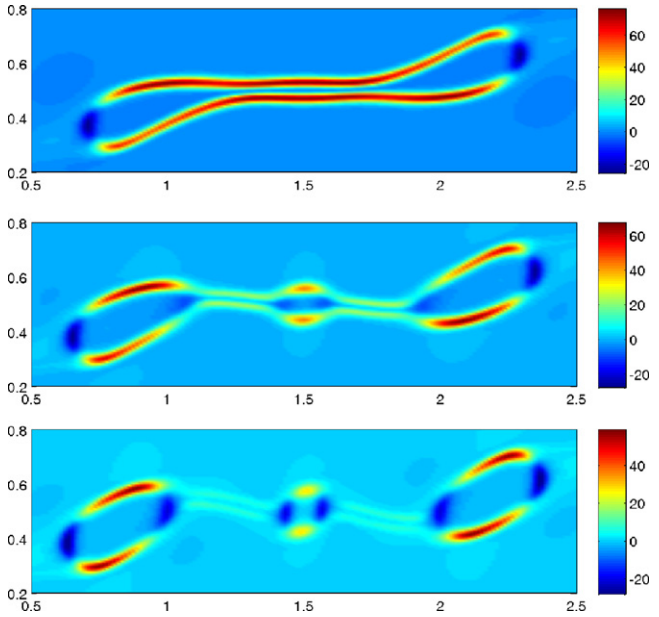

Fig. 12. First normal stress difference distributions $\sigma_{11} - \sigma_{22}$ corresponding to Figs. 9–11.

The capillary number in this model is defined by $Ca = \mu a \kappa / \sigma_{st}$ where the effective surface tension σ_{st} is identified in this diffuse interface model as $\sigma_{st} = (2\sqrt{2}\lambda/3\eta)$ in [86]. Note that the drop radius a is only well-defined in the early evolution of each simulation and after convergence to an equilibrium droplet distribution. The goal now is to compare the fate of the initial drop, the defects that form in the LC phase, the shear and normal stress distributions around deforming and stationary drops, and the secondary flow around the droplets, as we vary capillary number Ca (through the bulk shear rate κ), the LC bulk energy constant K and LC anchoring energy constant A.

The initial conditions for velocity and pressure are $(\mathbf{u}, p) = (u, v, p) = (\kappa(2y - H)/H, 0, 0)$. We prescribe the initial phase function to be $\phi = -\tan h(\sqrt{(x - 3H/2)^2 + (y - H/2)^2} - H/4/\eta)$, which is the equilibrium energy minimizer for this geometry [70].

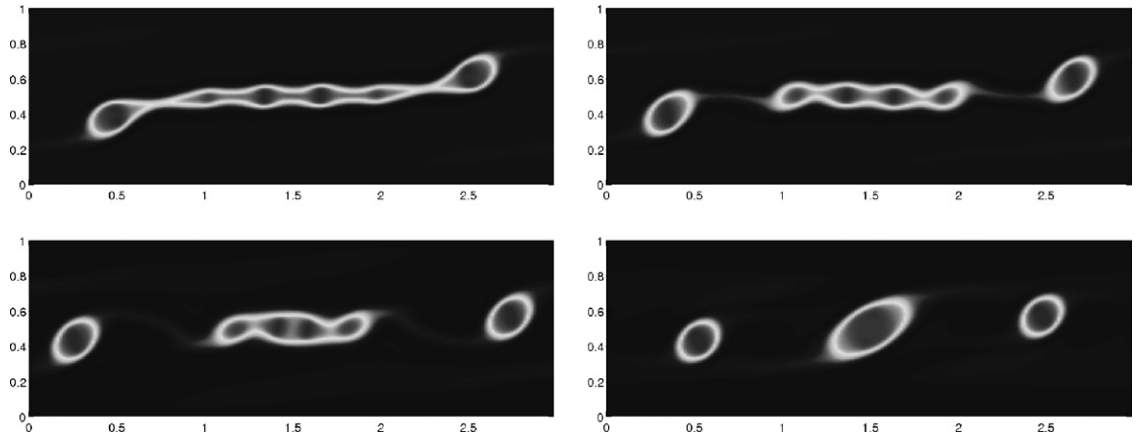

Fig. 13. Snapshots of the sheared liquid crystal drop with anchoring energy constant $A = 0.5$ at $t = 0.23, 0.3, 0.35, 0.75$.

As mentioned in the last section, the advantage of the numerical algorithm is that we only need to solve the following Poisson-type equations,

$$\begin{cases} u - \alpha\nabla^2 u = f, \\ u(x,y)|_{y=0,H_y} = 0 \text{ or } \dfrac{\partial u(x,y)}{\partial y}|_{y=0,H_y} = 0, \end{cases} \tag{4.1}$$

and the bi-harmonic equation

$$\begin{cases} u + \alpha_1\nabla^2\nabla^2 u - \alpha_2\nabla^2 u = f, \\ \dfrac{\partial u(x,y)}{\partial y}|_{y=0,H_y} = 0, \\ \dfrac{\partial^2 u(x,y)}{\partial y^2}|_{y=0,H_y} = 0. \end{cases} \tag{4.2}$$

We assume that the function $u(x, y)$ can be expanded in the following form, consistent with physical boundary values between the plates and periodicity in the flow direction,

$$u(x,y) = \sum_{n=-N/2}^{n=N/2} u_n(y) e^{inx}. \tag{4.3}$$

Insertion of the above form into (4.1) and (4.2), we obtain

$$\begin{cases} (1 + \alpha n^2)u_n(y) - \alpha\Delta u_n(y) = f_n(y), \\ u_n|_{(y=0,H_y)} = 0 \text{ or } u_n'(y) = |_{(y=0,H_y)} = 0, \end{cases} \tag{4.4}$$

$$\begin{cases} (1 + \alpha_1 n^4 + \alpha_2 n^2)u_n(y) + \alpha_1\nabla^2\nabla^2 u_n(y) \\ \quad -(\alpha_1 n^2 + \alpha_2)\nabla^2 u_n(y) = f_n(y), \\ u_n'(y) = u''_n(y)|_{(y=0,H_y)} = 0. \end{cases} \tag{4.5}$$

For any fixed n, we only need to solve the above 1D Poisson and bi-harmonic equations, for which we adopt the spectral-Galerkin method with Legendre polynomial basis [67]. The time step is set to be 10^{-5} and the spatial resolution consists of 512 Fourier modes and 512 Legendre modes.

4.2. The viscous drop in a viscous fluid benchmark

We start by simulating an immiscible viscous drop in another viscous fluid with the Cahn–Hilliard model. This is a limiting case of our model and algorithm, achieved by turning off both the bulk LC elastic energy ($K = 0$) and the LC anchoring energy ($A = 0$). The parameter set given above was determined by numerical exploration to recover published experimental and numerical behavior (cf. Ref. [9]), in a qualitative sense. Our model exhibits diverse rupture scenarios, which we do not show because they may be artifacts of the model in unphysical parameter regimes.

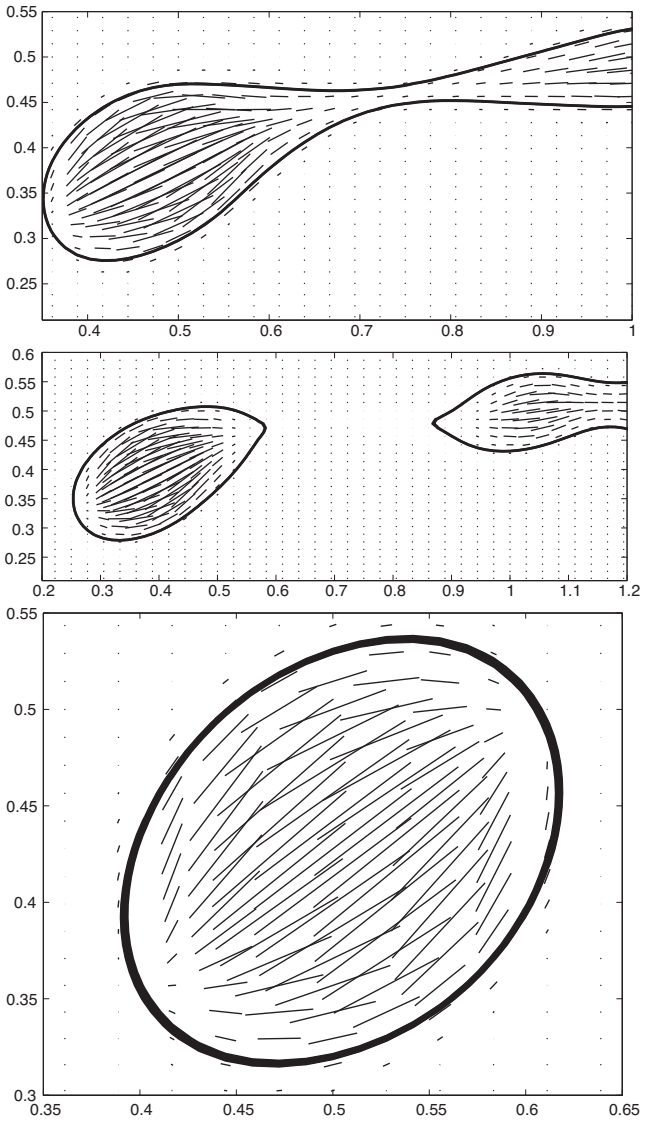

Fig. 14. A blow-up of the director field n from Fig. 13 at $t = 0.24, 0.28$, followed by a further blow-up of the droplet on the left at $t = 0.75$.

We note that we performed several tests to make sure that the drop breakup scenario was not strongly influenced by the effects of confinement. We reduced the drop area in half while holding the computational domain fixed, and we increased the size of the

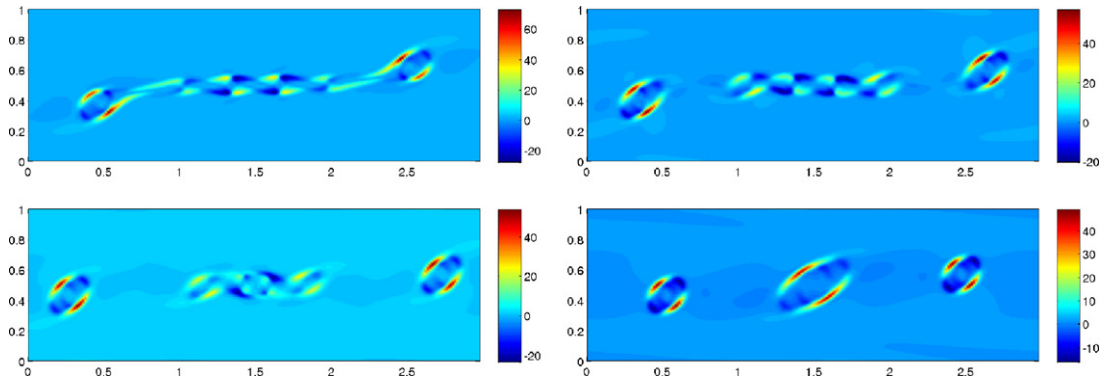

Fig. 15. Shear stress distributions corresponding to Fig. 13.

computational domain by a factor of 4 while holding the initial drop area fixed. The simulations that are presented here have a weak nonlinear shear at the sidewalls, whereas both reductions in drop area fraction lead to simple linear shear at the sidewalls but with the same drop breakup scenario. We omit these additional simulations, which are available upon request.

4.2.1. Sub-critical capillary number prior to drop breakup

First, for the fixed parameters indicated above, we numerically determine the critical capillary number $Ca \sim .0530$ corresponding to $\kappa \sim 12\,s^{-1}$, where the drop transitions from a steady equilibrium shape to breakup. Fig. 2 shows the steady drop shape for $\kappa = 15\,s^{-1}$ ($Ca = .0486$) (Figs. 3 and 4).

4.2.2. Super-critical capillary number and drop breakup

We now raise the shear rate to $\kappa = 15\,s^{-1}$ for which the capillary number $Ca = .0663$. Fig. 5 shows a sequence of snapshots as the droplet is sheared, elongated, develops a thin thread between two separating drops, and finally the thread breaks leaving two stable daughter droplets similar in shape and orientation to the subcritical capillary number prediction. The detailed hydrodynamics of the droplet deformation and rupture is given in Fig. 6, which superimposes the velocity field around the zero level set of the phase field function ϕ. The nonlinear shear and generation of vertical transport due to the Cahn–Hilliard dynamics are evident. Figs. 7 and 8 show level sets of the shear stress and first normal stress difference associated with the velocity field snapshots in Fig. 6. We define the shear and normal stress components with respect to the coordinates of the shear cell, where the "xy" or "12" component of σ is the primary shear stress, and the differences between the "xx" (11) and "yy" (22) components of σ define the first normal stress difference N_1. These stress features are standard metrics for shear rheology [35,45], so we will focus on the level sets of these stress features across the computational domain. We note that the most relevant coordinates to define shear and normal stress components for a viscoelastic fluid domain bounded by an evolving free surface are not standardized. In a neighborhood of the interface, the surface tangent and normal are most natural; however, our interfaces will rupture, rendering those coordinates problematic. We note that stable drops possess a symmetric distribution of positive and negative shear stress and first normal stress difference, which we shall call a quadrupolar stress distribution. Integration of these stresses over their respective domains leads to a balance of shear and normal forces that sustain a stable drop.

4.3. A liquid crystal drop immersed in a viscous fluid

We now study the shear-induced dynamics of a liquid crystal drop. In all computations reported below, we fix the bulk Frank elasticity constant $K = 0.05$ and then vary the strength of the anchoring energy A. The fixed parameter values imposed above for the viscous drop simulations are retained. We choose the super-critical shear rate $\kappa = 15\,s^{-1}$ and capillary number $Ca = .0663$ from the viscous drop simulation, since for different K and A the critical shear rate will change. We initialize a uniform director field $n = (1, 0)$ aligned with the direction of plate motion, and recall that our anchoring energy potential promotes tangential anchoring along the drop interface when $A > 0$. A similar study can be carried out with normal (homeotropic) anchoring at the drop interface, and with different Frank elasticity constant K, but those results are not considered here.

4.3.1. Frank elasticity in the LC phase with zero surface anchoring energy ($A = 0$)

Comparing Fig. 9 with Fig. 5, the elastic energy and extra stress in the LC domain have several consequences. The initial stretching and elongation of the LC drop is slower than the viscous drop. Next, the thinning thread of LC fluid does not "thin and break" in a truly longwave instability mechanism (which drains all fluid back into the two daughter drops). Instead, the thinning thread develops a capillary instability with a wavelength that supports the growth of one drop in the interior filament. The two threads that now connect the 3 emerging droplets follow the longwave rupture scenario observed in Fig. 5.

The upshot of this simulation is that an elasticity-induced instability saturates in the formation of an additional smaller satellite drop between the two daughter drops. Bulk Frank elasticity alone in the LC phase causes a transition from two to three droplets with all other material and experimental conditions held constant.

Fig. 10 superimposes the velocity field with the drop shapes at the same snapshots as in Fig. 9, while Figs. 11 and 12 show the shear and first normal stress distributions, respectively, for all three snapshots. Note that the stable daughter droplets each develop the quadrupolar stress distributions around their interface that were observed in stable viscous drops.

4.3.2. Frank elasticity in the LC phase with moderate surface anchoring energy ($A = 0.5$)

We now couple surface anchoring energy, which leads to a strong coupling of the phase field function ϕ with the LC orientation field n in both the flow equations (through the elastic extra stress) and the director evolution equation. Four snapshots are shown in Fig. 13. Rather than focus on early stretching dynamics, we focus instead on the subsequent rippled structure in the interior filament at $t = .23$. We observe that bulk elasticity coupled with interfacial anchoring energy contribute to a shorter wavelength capillary instability of the interior, stretching filament. Here, the wavelength is one-fourth of the length of the interior thread, which has the

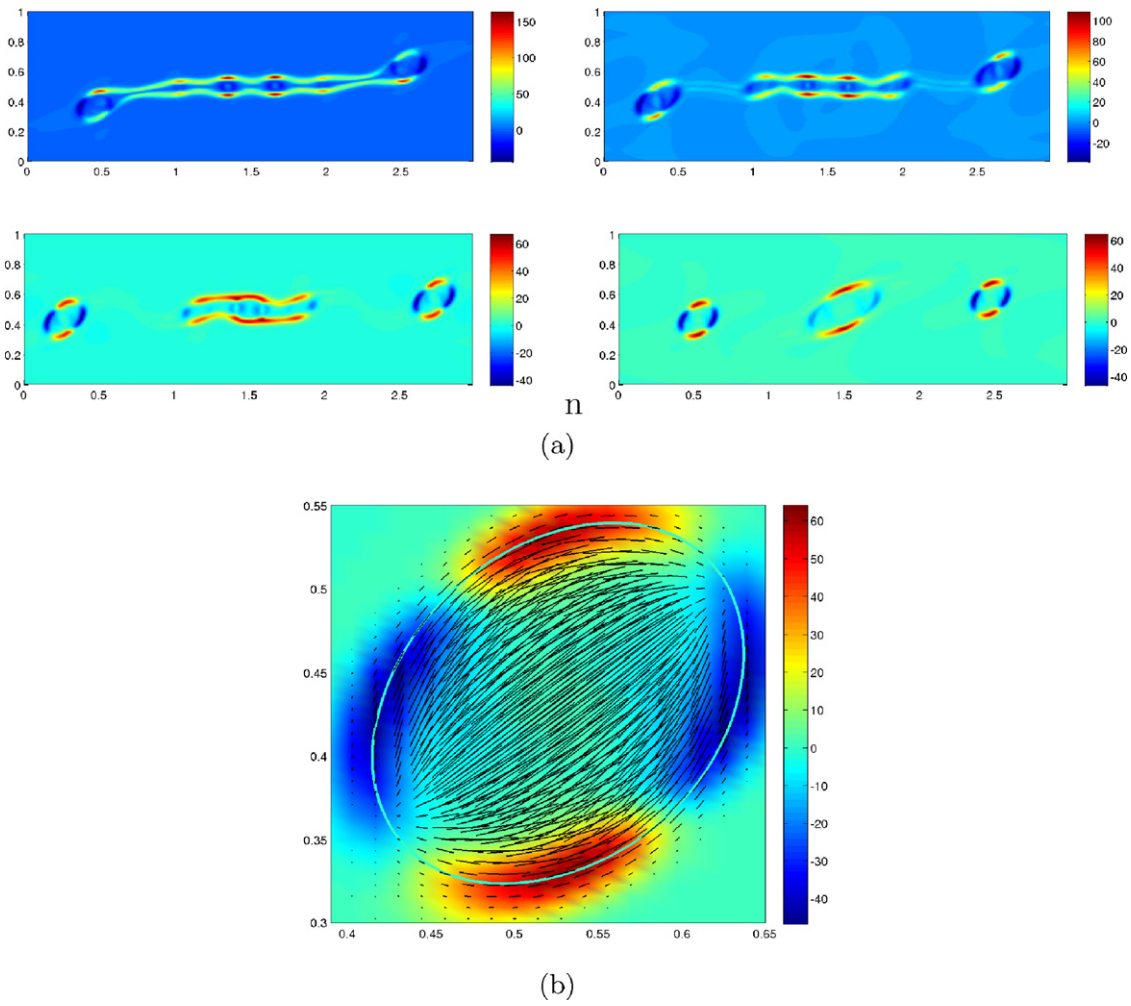

Fig. 16. (a) First normal stress difference $\sigma_{11} - \sigma_{22}$ corresponding to Figs. 13 and 15; (b) a blow-up of the droplet on the left in Fig. 14 with the director field n superimposed with the color-coded shear stress distribution $\sigma_{11} - \sigma_{22}$ at $t = 0.75$. (For interpretation of the references to color in this figure legend, the reader is referred to the web version of the article.)

effect of retaining significantly more mass in the interior thread than the $A = 0$ simulation. The instability of the interior thread once again does not grow; the perturbations are arrested, smooth out, and the interior mass recoils to form a single daughter droplet. The interior droplet is larger than the two droplets shed off the tips. The final outcomes for $A = 0$ and $A = 0.5$ are 3 daughter droplets each, but with different size distributions, and a very different transient dynamics.

We turn attention now to the LC orientation field, since this is the first simulation with LC physics in the bulk and diffuse interface. Fig. 14 is a blow-up of the left tip of the sheared droplet as the daughter droplet ruptures from the tip and then forms a stable small droplet; the LC director field is superimposed in each snapshot. The stable daughter droplet illustrates a numerical observation: *every daughter droplet has the same global bipolar defect structure, called a boojum, with two surface point defects of topological degree* $+1/2$ *and* $-1/2$ *situated at opposite poles of the equilibrium drop* [32,50,79]. Boojums are typical of tangential anchoring conditions on bounded volumes of LCs in equilibrium, whereas here they are the canonical orientation structure of steady state droplets in a steady shear-dominated 2D velocity field.

We turn now to the shear stress distribution (Fig. 15), first normal stress distribution (Fig. 16), and velocity field (Fig. 17) for each of the above snapshots. Once again, there is a clear shear and normal

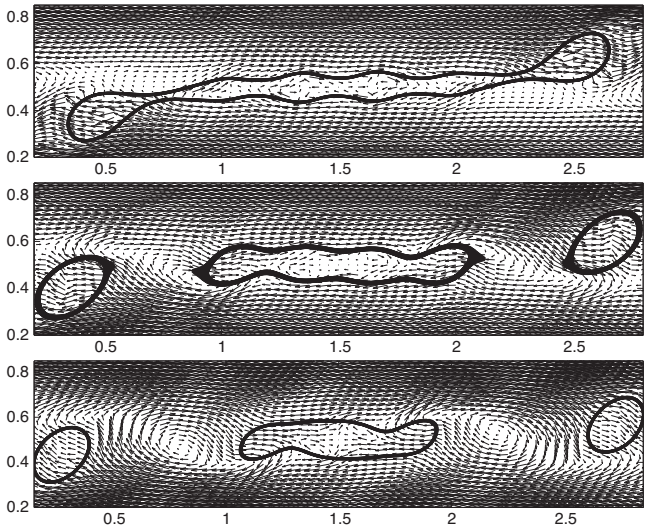

Fig. 17. The velocity field superimposed with the level set $\{x : \phi(x) = 0\}$ corresponding to Fig. 13.

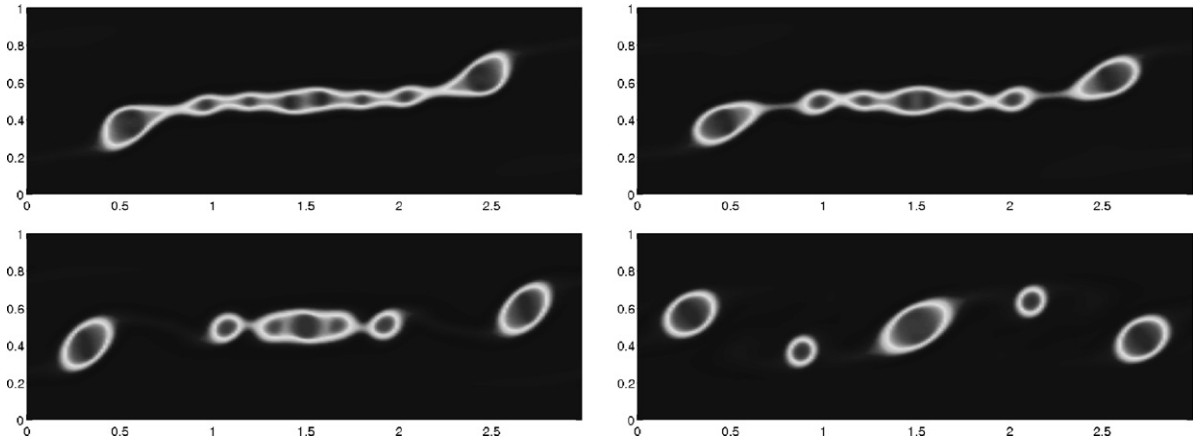

Fig. 18. Snapshots of a sheared liquid crystal drop with anchoring energy constant $A = 0.7$ at $t = 0.2, 0.23, 0.3, 0.45$.

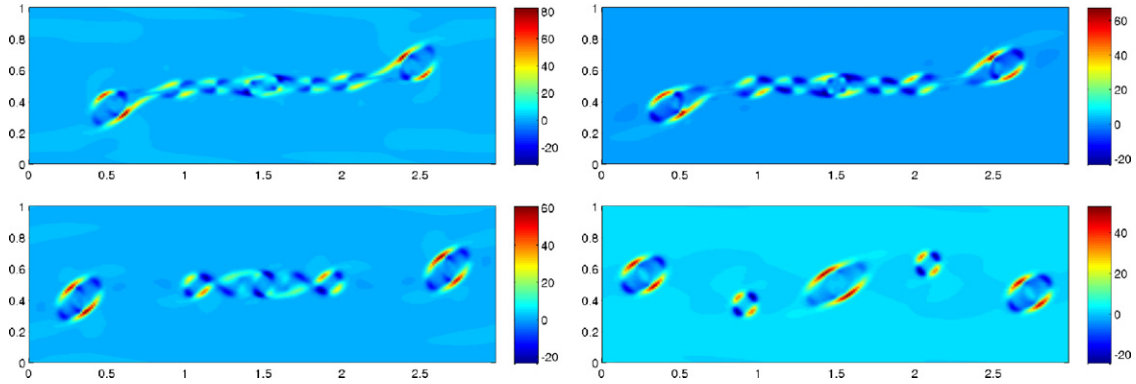

Fig. 19. Shear stress distributions σ_{12} corresponding to Fig. 18.

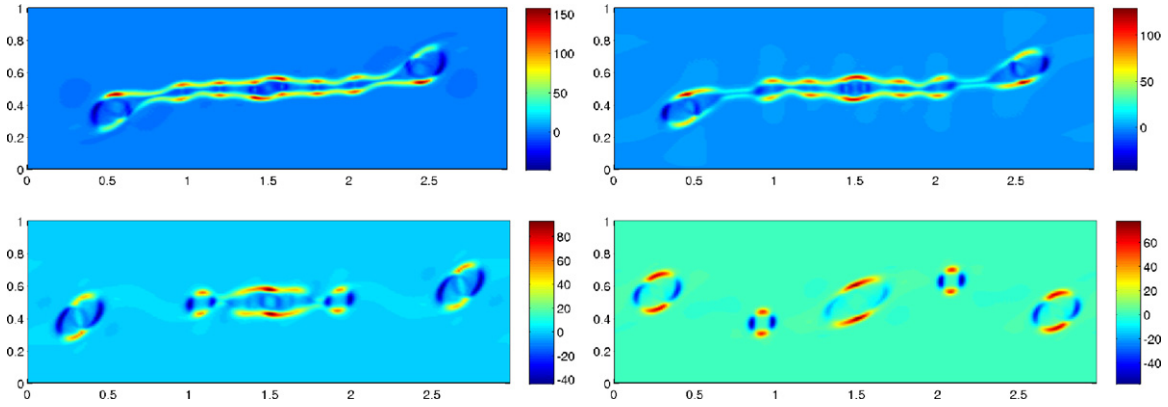

Fig. 20. First normal stress differences distributions $\sigma_{11} - \sigma_{22}$ corresponding to Figs. 18 and 19.

stress signature, the quadrupolar stress structure seen in all stable droplets, and the flow feedback due to the LC bulk and interfacial stress is clearly evident. Finally, we point to Fig. 16b that shows a remarkable feature. Namely, the two surface defects are located in the transition zones between positive and negative shear stresses and first normal stress differences. This global orientation-stress structure appears to characterize all steady LC drops.

The final simulation corresponds to a stronger surface anchoring energy, raising A to 0.7. Fig. 18 shows a similar early evolution, with stretching, shedding of droplets off the tips, and a rippled interior filament with 5 ripples instead of 4. The anchoring energy apparently tunes the wavelength of the elastic capillary instability of the interior thinning filament: stronger anchoring energy leads to onset of shorter wavelengths and the potential for different satellite drop formation scenarios. In this simulation, the interior rippled filament does not recoil as in the $A = 0$ and $A = 0.5$ simulations to form a third drop. Rather, the interior filament behaves similar to the original sheared drop, shedding drops from the ends, after which the interior ripples coarsen to form a fifth droplet. The final outcome consists of five daughter droplets of three different sizes. Figs. 19 and 20 show once again the shear and first normal stress distributions evolve to a quadrupolar structure in each steady state droplet, and the velocity distributions in Fig. 21 show stronger 2D flow feedback due to enhanced surface anchoring energy. All daughter droplets possess the global boojum defect structure, where the surface

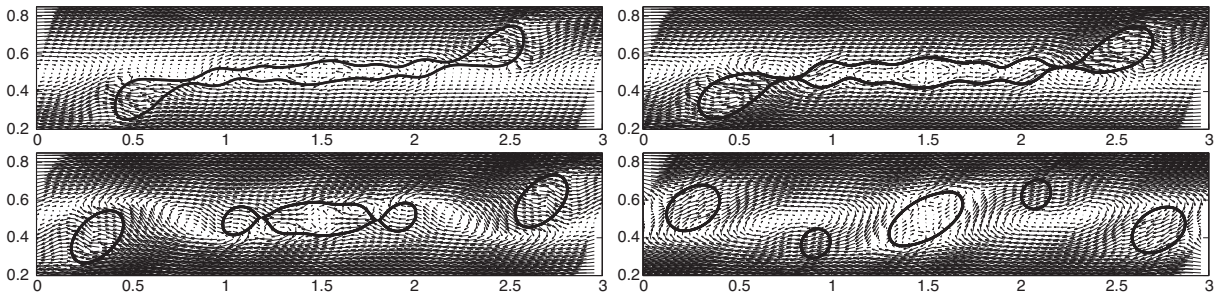

Fig. 21. The velocity field superimposed with the level set $\{x : \phi(x) = 0\}$ corresponding to Figs. 18–20.

defects reside at opposite poles in the transition regions from positive to negative shear stress and first normal stress differences.

5. Conclusion

An energy-based phase field model is presented for the dynamics of liquid crystal drops in an immiscible viscous fluid in a parallel-plate shear cell. A stabilized semi-implicit first-order time-marching scheme, coupled with a Fourier–Legendre–Galerkin approximation in two space dimensions, is implemented to study the deformation and rupture of the immersed LC (or viscous) droplet.

Numerical experiments are presented for the viscous drop problem to identify a critical capillary number for droplet breakup, and to identify parameter sets which reproduce the qualitative behavior of thin fluid threads connecting the two daughter drops when the drop ruptures. We then retain these parameters and explore the modified drop evolution at super-critical capillary number for a LC drop. We first introduce bulk Frank elasticity in the LC drop, while suppressing the interfacial anchoring energy. While not physically motivated, this simulation shows that bulk elasticity alone can lead to a different rupture scenario, in which a third, smaller satellite droplet forms through a capillary instability of the thread connecting the two emerging drops. We then turn on the anchoring energy which promotes tangential anchoring of the LC director along the interface, and further introduces an elastic stress contribution. This simulation leads to a shorter wavelength capillary instability of the filament connecting the bulging tips of the original sheared LC drop. The interior filament possesses more mass, so that the first two drops shed off the tips are smaller. The sheared interior filament either recoils to form one larger droplet or breaks up into more satellite drops, depending on the strength of the anchoring energy. Thus we find the ability to tune the number and size of daughter droplets by varying capillary number, Frank elasticity constant, and anchoring energy.

Along with each droplet rupture scenario, we show flow, stress and defect features. Frank elasticity and anchoring energy lead to significant 2D flow generation relative to the viscous drop simulations. Furthermore, all stable drops acquire the same symmetric shear and first normal stress difference distributions around the drop interface, with four strips of positive and negative stresses interlacing one another, which has a quadrupolar structure. Additionally, all stable LC drops with both Frank elasticity and anchoring energy potentials have a global bipolar defect structure called a boojum [49,32,50,79], with two opposite signed, half-integer degree defects at opposite poles of the stable drop. Remarkably, these surface defects reside precisely in the transition regions between positive and negative values of shear stress and first normal stress difference distributions. There are four such regions, but the drops are deformed ("squeezed") out of an equilibrium circular shape by the steady shear-dominated flow in the shear cell; the surface defects always reside in the two regions with greater curvature.

There are remaining issues which can be investigated using the current model and code, for example, the extensions of the model and code to a polymer solvent, adding viscous torques to the director equation, changing the anchoring conditions to favor normal anchoring which will promote internal hedgehog defects instead of the surface boojums, and generalizing the current Ericksen–Leslie model to more general liquid crystalline polymer tensor models. These investigations will be pursued elsewhere.

Acknowledgements

The research of X. Yang is partially supported by ARO W911NF-09-1-0389. The research of M.G. Forest is partially supported by NSF DMS-0908423, ARO W911NF-09-1-0389, and the Department of Energy. The research of C. Liu is partially supported by NSF-0707594. The research of J. Shen is partially supported in part by NSF-0915066 and AFOSR FA9550-08-1-0416.

References

[1] D. Adalsteinsson, J.A. Sethian, A fast level set method for propagating interfaces, J. Comput. Phys 118 (1995) 269–277.
[2] D.M. Anderson, G.B. McFadden, A.A. Wheeler, Diffuse-interface methods in fluid mechanics, Annu. Rev. Fluid Mech. 30 (1998) 139–165.
[3] P.E. Arratia, J.P. Gollub, D.J. Durian, Polymer drop breakup, Chaos 17 (2007) 041102.
[4] P.E. Arratia, J.P. Gollub, D.J. Durian, Polymer filament thinning & breakup in microchannels, Phys. Rev. E 77 (2008) 036309.
[5] G.K. Batchelor, An Introduction to Fluid Dynamics, Cambridge University Press, 1999.
[6] I.B. Bazhlekov, P.D. Anderson, H.E.H. Meijer, Nonsingular boundary integral method for deformable drops in viscous flows, Phys. Fluids 16 (4) (2004) 1064–1081.
[7] S. Bechtel, M.G. Forest, D. Holm, K Lin, 1-D closure models for 3-d incompressible viscoelastic free jets: von Karman flow geometry and elliptical cross-section, J. Fluid Mech. 196 (1988) 241–262.
[8] P.M. Chaikin, T.C. Lubensky, Principles of Condensed Matter Physics, Cambridge University Press, Cambridge, 1995.
[9] V. Cristini, J. Blawzdziewicz, M. Loewenberg, An adaptive mesh algorithm for evolving surfaces: simulations of drop breakup and coalescence, J. Comput. Phys. 168 (2001) 445–463.
[10] V. Cristini, Y.-C. Tan, Theory and numerical simulation of droplet dynamics in complex flows – a review, Lab chip 4 (2004) 257–264.
[11] M. Doi, S.F. Edwards, The Theory of Polymer Dynamics, Oxford University Press, United Kingdom, 1986.
[12] P.S. Drzaic, Free energy of a nonuniform system. I. Interfacial free energy, J. Chem. Phys. 28 (2005) 258–267.
[13] Q. Du, C. Liu, X. Wang, Simulating the deformation of vesicle membranes under elastic bending energy in three dimensions, J. Comput. Phys. 212 (2005) 757–777.
[14] D.A. Edwards, H. Brenner, D.T. Wasan, Interfacial Transport Process and Rheology, Butter-worths/Heinemann, London, 1999.
[15] J. Eggers, Theory of drop formation, Phys. Fluids 7 (1995) 941–953.
[16] J. Eggers, Nonlinear dynamics and breakup of free-surface flows, Rev. Mod. Phys. 69 (1997) 865–930.
[17] A. Fernandez-Nieves, D.R. Link, D. Rudhardt, D.A. Weitz, Electro-optics of bipolar nematic liquid crystal droplets, Phys. Rev. Lett. 92 (2004) 105503.

[18] R.W. Flumerfelt, Drop breakup in simple shear fields of viscoelastic fluids, Ind. Eng. Chem. Fundam. 11 (1972) 312–318.
[19] J. Glimm, M.J. Graham, J. Grove, X.L. Li, T.M. Smith, D. Tan, F. Tangerman, Q. Zhang, Front tracking in two and three dimensions, J. Comput. Math. 7 (1998) 1–12.
[20] M. Goldin, J. Yerushalmi, R. Pfeffer, R. Shinnar, Breakup of a laminar capillary jet of a viscoelastic fluid, J. Fluid Mech. 38 (1969) 689–711.
[21] J.L. Guermond, J. Shen, On the error estimates of rotational pressure–correction projection methods, Math. Comput. 73 (2004) 1719–1737.
[22] D. Gueyffier, J. Li, A. Nadim, R. Scardovelli, S. Zaleski, Volume-of-fluid interface tracking with smoothed surface stress methods for three-dimensional flows, J. Comput. Phys. 152 (1999) 423–456.
[23] S. Guido, M. Villone, Three dimensional shape of a drop under simple shear flow, J. Rheol. 42 (1998) 395–415.
[24] D.M. Henderson, H. Segur, L.B. Smolka, M. Wadati, The motion of a falling liquid filament, Phys. Fluids 13 (2000) 550–565.
[25] E.J. Hinch, A. Acrivos, Long slender drops in simple shear flow, J. Fluid Mech. 98 (1980) 305C328.
[26] C.W. Hirt, B.D. Nichols, Volume of fluid (VOF) method for the dynamics of free boundaries, J. Comput. Phys. 39 (1) (1981) 201–225.
[27] T.Y. Hou, Numerical study of free interface problems using boundary integral methods, in: Documenta Mathematica, Extra Volume – Proceedings of the International Congress of Mathematicians, III, 1998, pp. 601–610.
[28] A.S. Hsu, L.G. Leal, Deformation of a viscoelastic drop in planar extensional flows of a Newtonian fluid, J. Non-Newton. Fluid Mech. 160 (2009) 176–180.
[29] Y. Hyon, D. Kwak, C. Liu, Energetic variational approach in complex fluids: maximum dissipation principle, DCDS-A 26 (4) (2009) 1291–1304.
[30] P.J.A. Janssen, A. Vananroye, P. Van Puyvelde, P. Moldenaers, P.D. Anderson, Generalized behavior of the breakup of viscous drops in confinements, J. Rheol. 54 (2010) 1047–1060.
[31] D. Khismatullin, Y. Renardy, M. Renardy, Development and implementation of VOF-PROST for 3d viscoelastic liquid–liquid simulations, J. Non-Newton. Fluid Mech. 140 (1992) 120–131.
[32] S. Kralj, R. Rosso, E.G. Virga, Fingered core structure of nematic boojums, Phys. Rev. E 78 (2008) 031701.
[33] V.V. Krotov, A.I. Rusanov, Physicochemical Hydrodynamics of Capillary Systems, Imperial College Press, London, 1999.
[34] K. Verhulst, R. Cardinaels, P. Moldenaers, S. Afkhami, Y. Renardy, Influence of viscoelasticity on drop deformation and orientation in shear flow. Part 2. Dynamics, J. Non-Newton. Fluid Mech. 156 (2009) 44–57.
[35] R.G. Larson, The Structure and Rheology of Complex Fluids, Oxford University Press, 1999.
[36] B.I. Lev, V.G. Nazarenko, A.B. Nych, P.M. Tomchuk, Deformation and instability of nematic drops in an external electric field, JETP Lett. 71 (2000) 262–265.
[37] H. Li, U. Sundararaj, Does drop size affect the mechanism of viscoelastic drop breakup? Phys. Fluids 20 (2008) 053101.
[38] J. Li, Y. Renardy, M. Renardy, Numerical simulation of breakup of a viscous drop in simple shear flow with a volume-of-fluid method, Phys. Fluids 12 (2000) 269–282.
[39] Z. Li, K. Ito, The Immersed Interface Method – Numerical Solutions of PDEs Involving Interfaces and Irregular Domains, SIAM Frontiers in Applied Mathematics, 2006.
[40] C. Liu, J. Shen, A phase field model for the mixture of two incompressible fluids and its approximation by a Fourier-spectral method, Physica D 179 (3–4) (2003) 211–228.
[41] C. Liu, J. Shen, X. Yang, Dynamics of defect motion in nematic liquid crystal flow: modeling and numerical simulation, Commun. Comput. Phys. 2 (2007) 1184–1198.
[42] C. Liu, N.J. Walkington, Approximation of liquid crystal flows, SIAM J. Numer. Anal. 37 (2000) 725–741.
[43] M. Loewenberg, E.J. Hinch, Numerical simulation of a concentrated emulsion in shear flow, J. Fluid Mech. 321 (1996) 395–419.
[44] J. Lowengrub, L. Truskinovsky, Quasi-incompressible cahnchilliard fluids and topological transitions, R. Soc. Lond. Proc. Ser. A Math. Phys. Eng. Sci. 454 (1998) 2617–2654.
[45] C.W. Macosko, Rheology: Principles, Measurements, and Applications, VCH Publishers, Inc., New York, 1994.
[46] F.P. La.Mantia, Thermotropic Liquid Crystal Polymer Blends, Technomic, Lancaster, 1993.
[47] F. Mashayek, N. Ashgriz, A hybrid finite-element-volume-of-fluid method for simulating free surface flows and interfaces, Int. J. Numer. Meth. Fluids 12 (2005) 1363–1380.
[48] L.J. McWhirter, G.N. Patey, Molecular dynamics simulations of a ferroelectric nematic liquid under shear flow, J. Chem. Phys. 117 (2002) 8551–8564.
[49] N.D. Mermin, Physica (Utrecht) 90 B+C (1977).
[50] V.P. Mineev, G.E. Volovik, Planar and linear solitons in superfluid ^{3}He, Phys. Rev. B 18 (1978) 3197.
[51] N.F. Morrison, G.H. Oliver, Viscoelasticity in inkjet printing, Rheol. Acta 49 (2010) 619–632.
[52] P.K. Notz, O.A. Basaran, Dynamics and breakup of a contracting liquid filament, J. Fluid Mech. 512 (2004) 223–256.
[53] M.S.N. Oliveira, G.H. McKinley, Iterated stretching and multiple beads-on-a-string phenomena in dilute solutions of highly extensible flexible polymers, Phys. Fluids 17 (2005) 071704.
[54] S.J. Osher, R.P. Fedkiw, Level Set Methods and Dynamic Implicit Surfaces, Springer-Verlag, 2002.
[55] C.S. Peskin, The immersed boundary method, Acta Numer. 11 (2002) 1–39.
[56] J. Plateau, Statique experimental et theorique des liquides soumis aux seules forces moleculaires, Gauthier-Villars II (1873) 319.
[57] O.O. Prishchepa, A.V. Shabanov, V.Ya. Zyryanov, A.M. Parshin, V.G. Nazarov, Friedericksz threshold field in bipolar nematic droplets with strong surface anchoring, Phys. Fluids 84 (2007) 607–612.
[58] R.F. Probstein, Physicochemical Hydrodynamics: An Introduction, Wiley, New York, 1994.
[59] J.M. Rallison, The deformation of small viscous drops in shear flows, Annu. Rev. Fluid Mech. 16 (1984) 45–66.
[60] S. Ramaswamy, L.G. Leal, The deformation of a viscoelastic drop subjected to steady uniaxial extensional flow of a Newtonian fluid, J. Non-Newton. Fluid Mech. 85 (1999) 127–163.
[61] L. Rayleigh, On the instability of jets, Proc. Lond. Math. Soc. 10 (1878) 4–13.
[62] L. Rayleigh, On the theory of surface forces-II. Compressible fluids, Phil. Mag. 33 (1892) 209C220.
[63] M. Renardy, Some comments on the surface tension driven break-up (or the lack of it) of viscoelastic jets, J. Non-Newton. Fluid Mech. 51 (1994) 97–107.
[64] J.S. Rowlinson, B. Widom, Molecular Theory of Capillarity, Clarendon Press, Oxford, 1989.
[65] J.A. Sethian, Level Set Methods and Fast Marching Methods: Evolving Interfaces in Computational Geometry, Fluid Mechanics, Computer Vision, and Materials Science, Cambridge University Press, 1999.
[66] J. Shen, Efficient spectral-Galerkin method. I. direct solvers for second- and fourth-order equations by using Legendre polynomials, SIAM J. Sci. Comput. 15 (1994) 1489–1505.
[67] J. Shen, Remarks on the pressure error estimates for the projection methods, Numer. Math. 67 (1994) 513–520.
[68] J. Shen, X. Yang, An efficient moving mesh spectral method for the phase-field model of two-phase flows, J. Comput. Phys. 228 (2009) 2978–2992.
[69] J. Shen, X. Yang, Numerical approximations of Allen–Cahn and Cahn–Hilliard equations, Discrete Contin. Dyn. Syst.-A 28 (2010) 1669–1691.
[70] J. Shen, X. Yang, A phase-field model for two-phase flows with large density ratio and its numerical approximation, SIAM J. Sci. Comput. 32 (2010) 1159–1179.
[71] X.D. Shi, M.P. Brenner, S.R. Nagel, A cascade of structure in a drop falling from a faucet, Science 265 (1994) 219–222.
[72] L.B. Smolka, A. Belmonte, Charge screening effects on filament dynamics in xanthan gum solutions, J. Non-Newt. Fluid Mech. 137 (137) (2006) 103–109.
[73] M.C. Sostarecz, A. Belmonte, Beads-on-string phenomena in wormlike micellar fluids, Phys. Fluids 17 (2004) L67–L70.
[74] G.I. Taylor, The formation of emulsions in definable fields of flow, Proc. R. Soc. Lond. Ser. A. 146 (1934) 501–523.
[75] G. Tryggvason, B. Bunner, A. Esmaeeli, D. Juric, N. Al-Rawahi, W. Tauber, J. Han, S. Nas, Y.-J. Jan., A front-tracking method for the computations of multiphase flow, J. Comput. Phys. 169 (2) (2001) 708–759.
[76] V.T. Tsakalos, P. Navard, E.E. Peuvrel-Disdier, Deformation and breakup mechanisms of single drops during shear, J. Rheol. 42 (1998) 1403–1417.
[77] J. van der Waals, The thermodynamic theory of capillarity under the hypothesis of a continuous density variation, J. Stat. Phys. 20 (1893) 197–244.
[78] S. Veerapaneni, D. Gueyffier, G. Biros, D. Zorin, A boundary integral method for simulating the dynamics of inextensible vesicles suspended in a viscous fluid in 2d, J. Comput. Phys. 228 (7) (2009) 2334–2353.
[79] G.E. Volovik, O.D. Lavrentovich, Topological dynamics of defects: boojums in nematic drops, Zhurn. Eksp. Teor. Fiz. 85 (1983) 1997–2010.
[80] J.L. West, Liquid-crystalline polymers, ACS Symp. Ser. (1990).
[81] E.D. Wilkes, S.D. Phillips, O.A. Basaran, Computational and experimental analysis of dynamics of drop formation, Phys. Fluids 11 (1999) 3577–3598.
[82] S.M. Wise, J.S. Lowengrub, J.S. Kim, W.C. Johnson, Efficient phase-field simulation of quantum dot formation in a strained heteroepitaxial film, Superlattices Microstruct. 36 (2004) 293–304.
[83] Z.L. Xu, J. Glimm, Y.M. Zhang, X.F. Liu, A multiscale front tracking method for compressible free surface flows, Chem. Eng. Sci. 62 (13) (2007) 3538–3548.
[84] X. Yang, Error analysis of stabilized semi-implicit method of Allen–Cahn equation, Discrete Contin. Dyn. Syst.-B 11 (2009) 1057–1070.
[85] X. Yang, J.J. Feng, C. Liu, J. Shen, Numerical simulations of jet pinching-off and drop formation using an energetic variational phase-field method, J. Comput. Phys. 218 (2006) 417–428.
[86] P. Yue, J.J. Feng, C. Liu, J. Shen, A diffuse-interface method for simulating two-phase flows of complex fluids, J. Fluid Mech. 515 (2004) 293–317.
[87] P. Yue, J.J. Feng, C. Liu, J. Shen, Transient drop deformation upon startup of shear in viscoelastic fluids, Phys. Fluids 17 (2005) 123101.
[88] P. Yue, C. Zhou, J.J. Feng, Spontaneous shrinkage of drops and mass conservation in phase-field simulations, J. Comput. Phys. 223 (1) (2007) 1–9.
[89] J. Zhang, D.M. Eckmann, P.S. Ayyaswamy, A front tracking method for a deformable intravascular bubble in a tube with soluble surfactant transport, J. Comput. Phys. 214 (1) (2006) 366–396.
[90] L. Zhang, L.Q. Chen, Q. Du, Morphology of critical nuclei in solid state phase transformations, Phys. Rev. Lett. 98 (2) (2007) 265703.
[91] X. Zhang, O.A. Basaran, An experimental study of the dynamics of drop formation, Phys. Fluids 7 (1995) 1184–1203.
[92] B. Zhou, A.C. Powell, Phase field simulations of early stage structure formation during immersion precipitation of polymeric membranes in 2d and 3d, J. Membr. Sci. 268 (2) (2006) 150–164.